Optics & Laser Technology 191 (2025) 113283

Contents lists available at ScienceDirect

Optics and Laser Technology

journal homepage: www.elsevier.com/locate/optlastec

Full length article

Tailoring orbital angular momentum entanglement through inverse design based on gradient descent

Youngbin Na [a,b], Do-Kyeong Ko [a,b,*]

[a] Department of Physics and Photon Science, Gwangju Institute of Science and Technology, Gwangju 61005, Republic of Korea
[b] Research Center for Photon Science Technology, Gwangju Institute of Science and Technology, Gwangju 61005, Republic of Korea

ARTICLE INFO

Keywords:
Orbital angular momentum
Entanglement
Structured light
Inverse design
Laser beam shaping

ABSTRACT

High-dimensional quantum entanglement is an important resource for fundamental research and quantum technological application. Recently, the orbital angular momentum (OAM) of light has received much attention to realize high-dimensional quantum systems, and generating and manipulating the OAM entanglement has become an important topic. Here, we propose an inverse design technique to manipulate the OAM entanglement of the photon pair generated through spontaneous parametric down-conversion. The proposed technique directly tailors the OAM states of entangled photon pairs by shaping the incident pump beam. In particular, we construct a physics-informed model by leveraging the backpropagation algorithm and adhering to the overlap integral relation. Our model automatically optimizes diffractive masks, allowing the structured pump to quantitatively modulate the OAM distribution. The generation of maximally entangled states in different dimensions is demonstrated numerically and experimentally.

1. Introduction

High-dimensional entanglement of quantum systems, referred to as qudits, can provide extended possibilities such as increased information capacity, a higher noise resistance, enhanced security against eavesdropping, and stronger violation of Bell's inequalities [1–4]. Various photonic degrees of freedom, including photon number, path, and frequency, have been utilized to implement high-dimensional encoding in quantum information applications [4], and the spatial degree of freedom, notably the orbital angular momentum (OAM), have emerged as valuable photonic resources for quantum communication [5–7]. Indeed, the OAM has been actively studied by many researchers due to its infinite dimensional space and ease of scalability [3,8]. Light OAM is characterized by a helical phase of $\exp(il\varphi)$, where l is a topological charge that determines the OAM mode, and φ represents the azimuth angle in the cylindrical coordinate system [9]. These OAM beams carry an OAM of $l\hbar$ per photon, and the value of l is theoretically unbounded, providing high-dimensional quantum states. One common method to produce OAM entanglement in photonic systems is through a nonlinear optical process called spontaneous parametric down-conversion (SPDC) [10], where a higher-energy photon (pump) is converted into a pair of lower-energy photons (signal and idler) inside a nonlinear crystal. The OAM states of photon pairs generated in the nonlinear medium are described as a coherent superposition of mode combinations permitted by the conservation of OAM [10,11]. For example, if a pump photon has zero OAM, the OAM states of entangled photon pairs should be anti-correlated, which is expressed as $|\psi\rangle = \sum_l c_l |l\rangle_s |-l\rangle_i$. Here, c_l corresponds to the probability amplitude of finding a signal photon with l and an idler photon with $-l$ and is determined according to the overlap integral [12,13].

Although the OAM degree of freedom is theoretically unlimited and provides a high-dimensional space, the entangled states generated by Gaussian pump beams are generally suboptimal. For example, the generated states cannot be maximally entangled because the coefficients c_l decrease as l increases [14]. Thus, an additional procedure to manipulate the OAM distribution is required. One can equalize these weights using a postselection process known as Procrustean filtering [15] for obtaining a maximally entangled state (MES) [3,16]. However, the Procrustean method of entanglement concentration is performed through spatial mode filtering, which leads to the inevitable loss of photon flux. In addition, this cannot control the relative phase of the generated photon pairs. Another method for creating high-dimensional OAM entanglement is to use indistinguishability and path identity [17,18]. The proposed framework, termed entanglement by path, offers

* Corresponding author at: Department of Physics and Photon Science, Gwangju Institute of Science and Technology, Gwangju 61005, Republic of Korea.
E-mail addresses: bini0880@naver.com (Y. Na), dkko@gist.ac.kr (D.-K. Ko).

https://doi.org/10.1016/j.optlastec.2025.113283
Received 17 April 2025; Received in revised form 26 May 2025; Accepted 28 May 2025
Available online 9 June 2025

a high degree of customizability. Kysela et al. demonstrated the generation of 3-dimensionally entangled states and proposed a concept to incrementally increase the dimensionality of entanglement [18].

Meanwhile, some researchers have focused on the pre-processing method, implemented through the modification of the input pump structure [19–21]. Their methods are based on beam shaping techniques and the superposition of Laguerre-Gaussian (LG) modes. In contrast to the post-processing methods described above, these techniques directly modulate the coefficient c_{l_s,l_i} by appropriately preparing the relative phase and amplitude of the LG modes being superposed [20,21]. Indeed, using these techniques, they have successfully produced high-dimensional MESs with the spatial degree of freedom. Additionally, Lie *et al.* theoretically and experimentally demonstrated that an exponential pump profile can provide a broader spiral bandwidth compared to the conventional Gaussian pump [22]. Since these techniques do not require post-processing, such as Procrustean filtering, one can use the full photon flux produced by the SPDC process, making these methods efficient tools for generating entangled states with high brightness [19–21].

Despite the efficient control of OAM entanglement via pump beam shaping, there are still some limitations in realizing user-defined entanglement. In the case of using mode superposition [19–21], the condition on the single-Schmidt mode regime is necessarily considered, in advance. Moreover, the existing pre-processing methods require obtaining an analytic solution to the overlap integral. Although it seems simple, determining a proper pump structure is a challenging problem because the pump function affects not only one mode but all combinations. These factors make it difficult to improve the customizability of the pre-processing techniques. In this paper, we present a programmable photonics source for OAM entanglement. The proposed method is similar to the aforementioned pre-processing techniques [19–22] in that it uses a structured pump. However, the optimized pump structure is automatically obtained through inverse design of diffractive elements. Specifically, we developed a physics-informed model based on gradient descent and the overlap integral relation. Through iterative process, our model computes a diffractive mask that shapes the pump for a given input beam and a target OAM distribution. To experimentally verify the proposed scheme, we generated MESs in different dimensions and investigated the generated quantum states by performing projective measurements and quantum state tomography (QST).

2. Physical principle and method

2.1. Orbital angular momentum states of entangled photon pair

SPDC is a nonlinear optical process that converts a higher-energy pump photon into a pair of lower-energy photons (signal and idler) according to energy conservation and momentum conservation. Assuming that the pump, signal, and idler photons are monochromatic, the photon pairs generated through the SPDC are described by [14]

$$|\psi\rangle = \int d\boldsymbol{q}_s d\boldsymbol{q}_i \varepsilon_P(\boldsymbol{q}_s + \boldsymbol{q}_i)\Phi(\boldsymbol{q}_s, \boldsymbol{q}_i)|\boldsymbol{q}_s\rangle|\boldsymbol{q}_i\rangle, \tag{1}$$

where $\boldsymbol{q}_s$ and $\boldsymbol{q}_i$ represents the transverse wave vectors of the signal and idler photons, $\varepsilon_P(\boldsymbol{q}_s + \boldsymbol{q}_i)$ is the pump field in the spatial frequency domain, and $|\boldsymbol{q}_k\rangle$ is the photon state with transverse wave vector $\boldsymbol{q}_k$. Here, the function $\Phi(\boldsymbol{q}_s, \boldsymbol{q}_i)$ results from the phase-matching condition and takes the form of a sinc function [14].

Meanwhile, the OAM states originating from the SPDC can be described using the LG mode set, which is expressed as [14,21]

$$|\psi\rangle = \sum_{l_s,p_s}\sum_{l_i,p_i} c^{l_s,l_i}_{p_s,p_i} |l_s, p_s\rangle |l_i, p_i\rangle. \tag{2}$$

Here, $c^{l_s,l_i}_{p_s,p_i}$ corresponds to the probability amplitude for finding a signal photon in the (l_s, p_s) mode and an idler photon in the (l_i, p_i) mode, i.e., $\sum^{l_s,l_i}_{p_s,p_i} \left|c^{l_s,l_i}_{p_s,p_i}\right|^2 = 1$. $\left|c^{l_s,l_i}_{p_s,p_i}\right|^2$ represents the relative weight of each mode, which in experiments is normalized by the maximum count. Assuming the conditions of the paraxial approximation and perfect collinear phase matching, the coefficient is calculated by the overlap integral:

$$c^{l_s,l_i}_{p_s,p_i} = \langle l_s, p_s; l_i, p_i|\psi\rangle = \iint r dr d\varphi E_p(r,\varphi)\left[\mathrm{LG}^{l_s}_{p_s}(r,\varphi)\right]^*\left[\mathrm{LG}^{l_i}_{p_i}(r,\varphi)\right]^*. \tag{3}$$

Here, (r, φ) represents the transverse coordinates in the cylindrical coordinate, $E_p(r, \varphi)$ is the field distribution of the used pump beam, and $\mathrm{LG}^l_p(r, \varphi)$ is the normalized LG mode function [9]:

$$\mathrm{LG}^l_p(r,\varphi) = C\left(\frac{\sqrt{2}r}{w_0}\right)^{|l|}\exp\left(-\frac{r^2}{w_0^2}\right)L^{|l|}_p\left(\frac{2r^2}{w_0^2}\right)\exp(il\varphi), \tag{4}$$

where C is the normalization constant, w_0 is the waist size of the fundamental mode, and $L^{|l|}_p$ represents the generalized Laguerre polynomials. In other words, the OAM distribution of entangled photon pairs can be controlled by pump beam parameters. In addition, considering the experimental situation using single-mode fibers (SMFs) for detection, we used the integral relation including the Gaussian functions $G(r; w_{\mathrm{SMF}})$ [12]:

$$c^{l_s,l_i}_{p_s,p_i} \propto \iint r dr d\varphi E_p(r,\varphi)\left[\mathrm{LG}^{l_s}_{p_s}(r,\varphi)\right]^*\left[\mathrm{LG}^{l_i}_{p_i}(r,\varphi)\right]^* G^2(r; w_{\mathrm{SMF}}). \tag{5}$$

Here, w_{SMF} is the size of the Gaussian function when imaged back onto the crystal plane. Meanwhile, since we are interested in manipulating OAM entanglement, we set the radial mode index p to 0 throughout the work without loss of generality. Note that the proposed inverse design scheme is independent of the mode selection. By considering non-zero radial index in our model, radial and OAM degrees of freedom are controlled simultaneously.

2.2. Inverse design based on gradient descent

Fig. 1 illustrates the concept of the inverse design-based entanglement control method. Our method provides a structured pump at the crystal plane by optimizing diffractive masks. An incident laser beam serves as the input to the modulation layer, and the beam modulated by the diffractive mask propagates [23,24]. At this time, the phase values of each mask correspond to the weight parameters that are updated. As shown in Fig. 1(b), given an input beam shape and a desired OAM spectrum, the model automatically finds optimized phase masks $\phi(m,n)$ by training. Specifically, the output shape takes the form of $N \times N$ matrix whose elements correspond to the values of $|c_{l_s,l_i}|^2$. For example, if we want to generate a 3-dimensional MES $|\psi\rangle = (|1,1\rangle + |0,0\rangle + |-1,-1\rangle)/\sqrt{3}$, a 3×3 identity matrix is given as the output answer. After propagation through all optical elements, the final layer of our model numerically calculates the overlap integral according to Eq. (5). The weight parameters are then updated with a gradient descent algorithm, minimizing the difference between the desired output and the calculated one [25].

Each optical element, such as modulation, propagation, and the overlap integral operation, was realized using a custom layer class in the Keras (2.10.0) framework in Python (3.7). The "OptModul" represents a modulation layer which modulates the incoming field by multiplying a phase mask ϕ, i.e., $u(x,y) = u_0(x,y)\exp[i\phi(x,y)]$. Free-space propagation is implemented in the "ASProp" layer using the angular spectrum method, which is expressed as [24,26,27]

$$Y = F^{-1}\left\{F\{u(x,y)\}\exp\left[id\sqrt{k^2 - 4\pi^2\left(f_x^2 + f_y^2\right)}\right]\right\}. \tag{6}$$

Here, F and F^{-1} represent the Fourier transform operation, $u(x,y,z)$ is the input field, d is the distance to the next layer, $k = 2\pi/\lambda$ is the

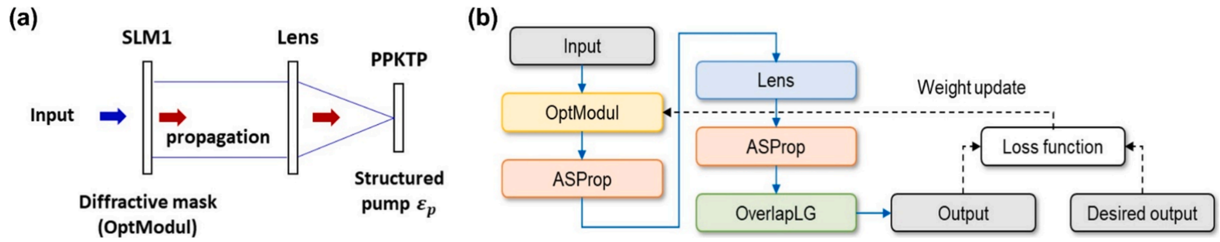

Fig. 1. Schematic diagram for tailoring OAM entanglement. (a) System configuration in the experiment and (b) the corresponding numerical model for optimization: SLM, spatial light modulator, OptModul, diffractive layer ϕ_i modulating an incident field; ASProp, propagation layer implemented using the angular spectrum method; OverlapLG, a layer for calculating the overlap integral.

wavenumber, and $\left(f_x, f_y\right)$ correspond to the spatial frequency components. Then, a pair of the "Lens" and "ASProp" layers focuses the modulated pump beam into the nonlinear crystal, and the "OverlapLG" layer calculates the overlap integral to provide the output. The size of the calculation window was set to 2000×2000 with a resolution of 4 μm, and 2×2 binning was applied to the diffractive mask to match the pixel size of the SLM (8 μm). The size of the diffractive mask is same as the size of the calculation window, and the number of diffractive neurons is 4 million. 30 Gaussian beams were used as input data for training, each with random displacements and variations in waist size. We trained the model for 1200 epochs with a batch size of 5 using a desktop computer (CPU: i5-13600 K; GPU: RTX 4090; RAM: 64 GB). We used RMSprop [28] as an optimization algorithm and mean-squared error (MSE) as the loss function. The learning rate was set to start at 0.1 and decrease to 1/10 if the loss did not improve for 150 epochs. Finally, we experimentally generated entangled photon pairs using the optimized phase mask and performed projective measurements to verify the results.

2.3. Experimental setup and details

Fig. 2 shows the experimental setup designed to verify the proposed scheme. A laser beam emitting from a 405 nm single-frequency diode laser (TopMode 405, TOPTICA Photonics) is used as the pump source for the SPDC process. With a pixel pitch of 8 μm, first SLM (PLUTO-2.1, Holoeye) displays a phase mask obtained through model training. Then, the pump beam is modulated by the SLM1 and focused into the nonlinear crystal (15 mm length type-II PPKTP, Raicol Crystals) by a lens of 150 mm focal length. When training the model, we applied a circular mask with $r = 0.5$ mm to employ the central region of the pump field; see the phase mask ϕ in Fig. 2. This is to reduce some artifacts resulting from the imperfect beam quality. Note that in the experiment a phase grating is included in the phase hologram to extract the modulated beam. After the crystal, an 810 nm bandpass filter with a full width at half maximum (FWHM) of 10 nm blocks the remaining pump photons. Each down-converted photon (signal and idler) is directed along different paths split by a Wollaston prism and a right angle prism. Then, the projective measurement on signal and idler photons is performed using the SLM2 followed by SMF-coupled single-photon detectors [12,13,20,21]. Photon arrival times are recorded by a time-correlated single photon counting (TCSPC) unit (MultiHarp 150, PicoQuant), and coincidence events are measured with a coincidence window of 10 ns. Here, each pair of lenses (L2-L3, and L4-L5 & L6-L7) is used to image from the crystal plane onto the SLM2 and from the SLM2 onto the end of each SMF. As a result, when imaged back onto the crystal plane, the waist size of the LG mode is $\sim$ 72 μm, and w_{SMF} corresponds to $\sim$ 100

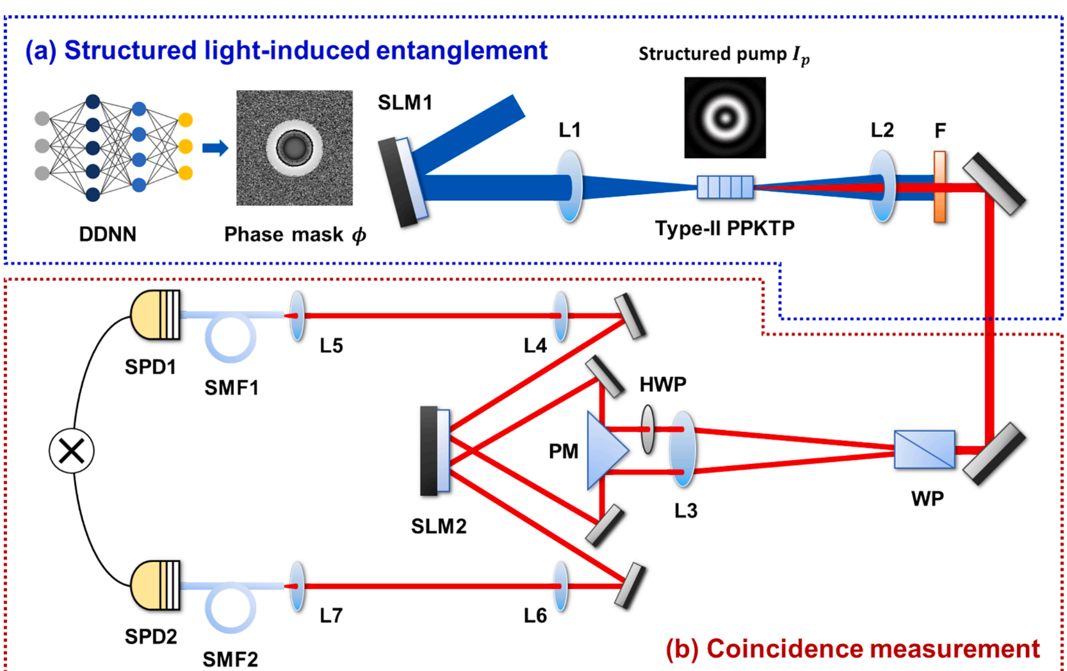

Fig. 2. Schematic diagram of the experimental setup: 405 nm pump source; SLM, spatial light modulator; L, lens; F, bandpass filter; WP, Wollaston prism; HWP, half wave plate; PM, leg-coated right-angle prism mirror; SMF, single-mode fiber; SPD, single-photon detector. An additional lens pair, not illustrated here, is placed to relay the image between two sections (a) and (b). The HWP after the L3 converts vertical polarization to horizontal polarization.

μm. Additionally, to optically implement the product of a mode function given in Eq. (5), we employed an amplitude-encoded phase function of the following form [21]:

$$\Phi_{\text{holo}}(x,y) = \exp[i\,\text{sinc}\,\pi(M(x,y)-1)\theta(x,y)]. \tag{7}$$

Here, $M(x,y)$ corresponds to the amplitude function of LG mode given in the range [0, 1]. $\theta(x,y)$ is the total phase profile expressed as $\theta(x,y) = \Phi_g + \text{Arg}\left(\text{LG}^{l}_{p=0}\right)$ [29], where $\Phi_g = 2\pi/\Lambda_g$ is the phase grating with a grating period Λ_g, and $\text{Arg}\left(\text{LG}^{l}_{p=0}\right)$ represents the phase distribution of the LG mode.

3. Results and discussion

3.1. Manipulation of high-dimensional OAM entanglement

Fig. 3 displays the training result for generating a 5-dimensional MES in our setup. The graph in Fig. 3(a) shows the MSE loss as a function of training epochs. In the early stage, up to around 460 epochs, the loss function exhibits a significant fluctuation, indicating a large initial deviation from the output answer. However, after around 460 and 740 epochs, the loss value drops rapidly, and the model starts to find appropriate parameters. As training progresses, the loss function converges to near-zero (5.34×10^{-5}), demonstrating that our model has effectively minimized the error and reached a stable solution. In other words, the phase distribution, which initially follows a random pattern, is iteratively updated, allowing the algorithm to find suitable weights and generate a customized pump structure; see the insets in Fig. 3(a). The red and blue bars in Fig. 3(b) represent $\left|c^{l_s,l_i}_{0,0}\right|^2$ calculated through numerical simulation. It is evident that the OAM spectrum, which initially peaks at the (0, 0) mode, becomes equalized through the structured pump beam.

Then, to experimentally verify the proposed scheme, we loaded an optimized mask into the SLM1 in our setup and conducted projective measurements. Fig. 4 shows normalized OAM spectra obtained from simulations and experiments. Provided equal weights $1/\sqrt{N}$ in a desired dimension, as the output answer, our model automatically finds an optimized phase distribution, i.e., an optimal pump structure, generating the target state. As shown in Fig. 4(a) and 4(b), the phase masks have no angular dependence, implying that total OAM is zero, and entangled photon pairs are anti-correlated in OAM. Measured OAM spectra are illustrated in Fig. 4(c) and 4(d). Here, we measured coincidence counts per each combination and normalized them by dividing the maximum value. There exist some discrepancies in the measured spectra, but it can be seen that 3 ($|1,-1\rangle$, $|0,0\rangle$, and $|-1,1\rangle$) and 5 ($|2,-2\rangle$, $|1,-1\rangle$, $|0,0\rangle$, $|-1,1\rangle$, and $|-2,2\rangle$) mode combinations approximate maximal, equal weights. Note that photon pairs generated without the help of inverse design in our setup have a sharp peak at $|0,0\rangle$; see Fig. 3(b). The deviations arise from three main issues: misalignment and aberrations of optical elements, and imperfect mode overlaps. Indeed, there are some distortions in the pump shape compared to our numerical predictions. These problems would be alleviated by performing precise alignment and wavefront correction. For the OAM state with 5 maximum equal weights, the coincidence count rate of $|0,0\rangle$ mode was measured to be $230\,\text{s}^{-1}\text{mW}^{-1}$. Most of the losses in our system occur from the modulation efficiency of the SLM2 ($<40\,\%$) and the collection efficiency of the fiber coupled SPD ($<30\,\%$). Additionally, the conversion efficiency of the phase mask obtained from our model was found to be $\sim 67\,\%$ for 3-dimensional MES. An additional loss function that calculates the power difference between the initial pump and the generated structured pump can improve the efficiency of diffractive masks. Using the hybrid loss function, the diffraction efficiency is shown to increase by about 10 %.

Finally, to characterize and examine generated quantum states, we performed QST and reconstructed density matrices for 2- and 3-dimensional MESs. Here, mutually unbiased bases were set for QST. Additionally, maximum likelihood estimation (MLE) was used to ensure that the reconstructed density matrices satisfy the physical criteria [21,30,31]. The optimization process is implemented minimizing the likelihood function of the form [30]

$$L(t_1,t_2,\cdots,t_m) = \sum_{i=1}^{m} \frac{\left[N\langle\psi_i|\rho_p|\psi_i\rangle - n_i\right]^2}{2N\langle\psi_i|\rho_p|\psi_i\rangle}, \tag{8}$$

where m is the number of measurements for reconstructing density matrices, N is the normalization constant, ρ_p is the physical density matrix, and n_i corresponds to the measured coincidence counts. The real and imaginary parts of the resulting density matrices are displayed in Fig. 5, where transparent bars represent theoretical values for the target MESs. Fig. 5(a)-5(c) correspond to the case of 2-dimensional MES $|\psi\rangle = \left(|1,1\rangle + e^{i\alpha}|-1,-1\rangle\right)/\sqrt{2}$, where $\alpha = -2.313$ is the relative phase. From the pump distribution, one can confirm that the entangled state originates from a superposition of two OAM modes ($l_p = \pm 2$) [20,21]. Fig. 5(d)-5(f) shows the case of 3-dimensional MES $|\psi\rangle = \left(e^{i\alpha_1}|1,-1\rangle + |0,0\rangle + e^{i\alpha_2}|-1,1\rangle\right)/\sqrt{3}$, where $\alpha_1 = \alpha_2 = 0.062$. The measured fidelity $F(\rho,\rho_{\text{exp}}) = \left[\text{Tr}\sqrt{\sqrt{\rho}\,\rho_{\text{exp}}\sqrt{\rho}}\right]^2$ of 2- and 3-

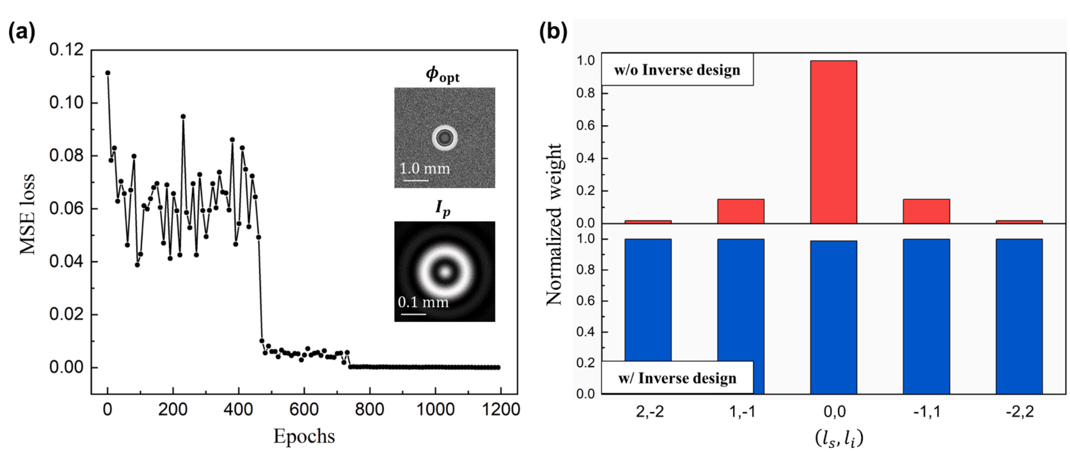

Fig. 3. Optimization results to generate an anti-correlated 5-dimensional MES. (a) Loss curve as a function of the number of iterations. To improve readability and highlight the overall trend, we plotted the loss function at every 10th epoch instead of showing the entire set of 1200 points. The insets show the optimized phase mask and corresponding pump distribution. (b) Spiral spectrum obtained with and without inverse design. Normalization was performed by dividing the maximum value.

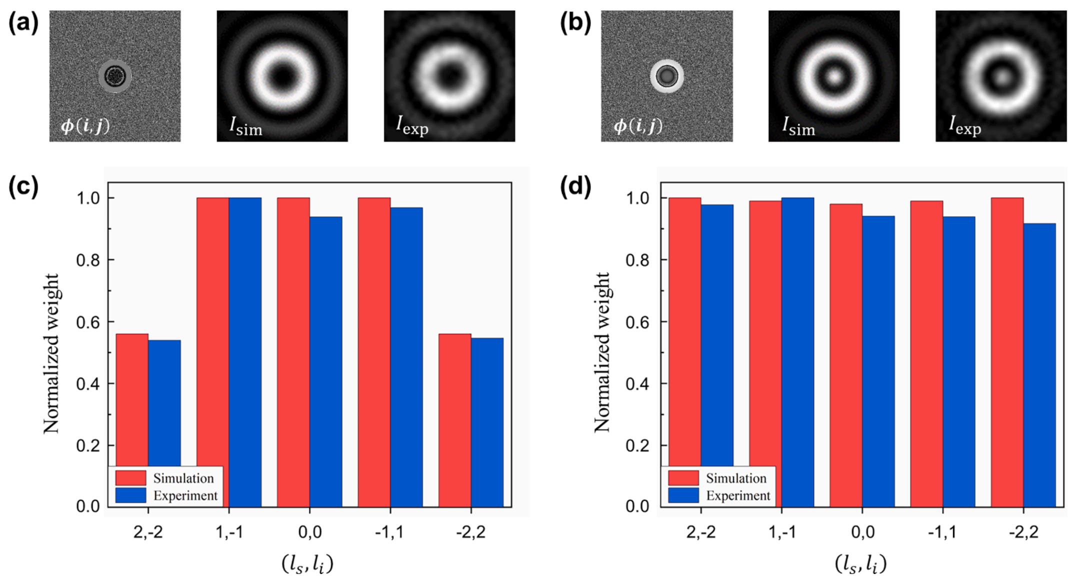

Fig. 4. Inverse design-based manipulation of OAM entanglement. (a), (b) Optimized phase masks and pump distributions for generating OAM states with 3 and 5 maximum equal weights. (c), (d) Corresponding normalized (divided by the maximum value) OAM spectra.

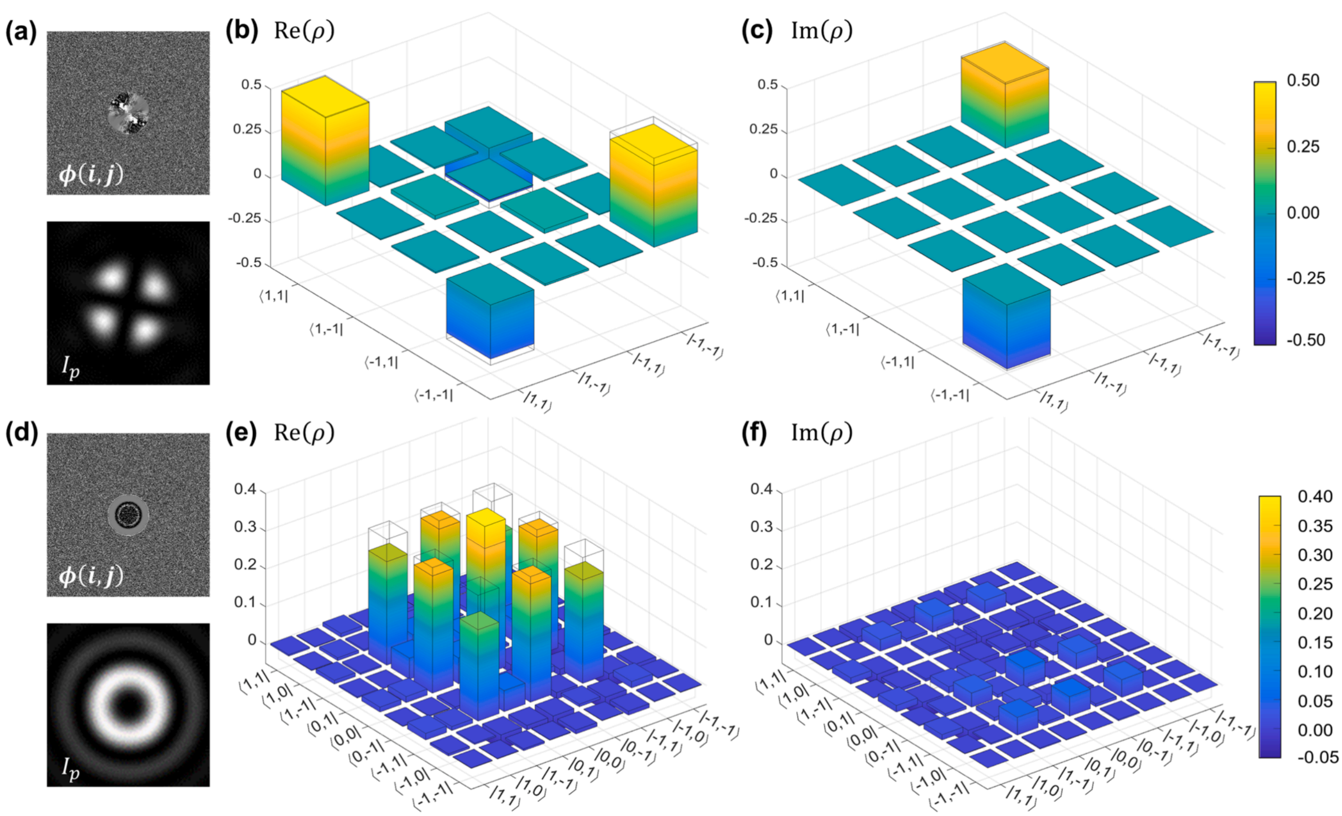

Fig. 5. Characterization of MESs realized in 2- and 3-dimensional subspaces. (a), (d) used phase masks and simulated pump distributions for generating the target states. (b), (e) real and (c), (f) imaginary parts of reconstructed density matrices. Here, overlaid bars depict corresponding theoretical values. The measurement time was set to 5 s for each mode.

dimensional MESs was 0.944 ± 0.007 and 0.889 ± 0.003, respectively. The uncertainty was estimated by statistical simulation assuming that coincidence events follows a Poisson distribution [21,22]. In addition, the linear entropy $S_L = 1 - \mathrm{Tr}\left(\rho_{\mathrm{exp}}^2\right)$ of 2- and 3-dimensional cases was measured to be 0.105 ± 0.013 and 0.116 ± 0.007, respectively. Meanwhile, our numerical simulation shows that the fidelity of the reconstructed density matrices is close to 1, which indicates that some experimental factors caused errors between the experiment and theoretical prediction. The reliability of the proposed method will be improved by introducing additional adaptive techniques. Furthermore, optimizing the masks with experimentally measured outputs could be one option to mitigate the errors.

We have demonstrated the controllability of the relative weights of entangled states. However, for practical applications, the ability to manipulate relative phases is also necessary. To achieve this, one can apply a multi-layered and multi-output model that accounts for both the relative phase and amplitude in the output. Specifically, the output matrices O_{abs} and O_{pha} represent the absolute values and phases of the complex coefficients c_{l_s,l_i}, respectively. For instance, to generate a 5-dimensional MES with no phase difference, i.e., the output desired state of $|\psi\rangle = (|2,2\rangle + |1,1\rangle + |0,0\rangle + |-1,-1\rangle + |-2,-2\rangle\ )/\sqrt{5}$, we select a 5×5 identity matrix for O_{abs} and a 5×5 zero matrix for O_{pha}. Meanwhile, increasing the number of layers, i.e., increased weight parameters, enables the model to learn more abstract representations, enhancing performance over complex problems [25]. Additionally, for entangled states generated by a pump beam in a superposition of several pure LG modes, relative phases can be controlled easily by global rotation of the pump beam [20,21,32]. Note that the 2-dimensional MES given in Fig. 5 corresponds to such case, and the relative phase α of that state can be adjusted by rotating the phase hologram displayed on the SLM1.

3.2. Effects of experimental factors

Because there are some practical issues affecting the performance in real experiments, we need to know the robustness of the designed systems. We first analyzed performance degradation under two types of misalignment: lateral displacement of the diffractive mask and axial mispositioning of the nonlinear crystal. Fig. 6 illustrates the changes in pump distribution and the resulting OAM spectrum in the presence of misalignment. Both types of offsets distort pump structure and cause deviations in the OAM spectrum. As the displacement from the ideal position increases, the initial OAM spectrum exhibiting equal weights for the three states $|1,-1\rangle$, $|0,0\rangle$, and $|-1,1\rangle$ gradually transforms into a distribution with a noticeable peak at $|0,0\rangle$. In addition, we explored the influence of input beam size w_p; see Fig. 7. As the beam size increases ($\Delta w_p > 0$), we observe an increase in the population of higher-order modes, particularly $|1,-1\rangle$ and $|-1,1\rangle$. In contrast, for $\Delta w_p < 0$, where the pump beam size is smaller than the intended size, the $|0,0\rangle$ becomes dominant. As shown in Fig. 7(b), these changes in the OAM spectrum correspond to increasing MSE values, indicating that any deviation from the optimal pump beam size leads to increased spectral distortion.

In other words, matching the input parameters to the intended values is crucial, and enhancing system stability in response to such problems is necessary. To increase the robustness of the system, the concept of data augmentation may be adopted [26,33,34]. Data augmentation is a technique of artificially generating new data from existing datasets by applying various transformations. This approach aims to increase the dataset size and prevent overfitting, thereby improving generalization ability of the model. For instance, input beams with slight variations in parameters, such as beam size and displacement from the beam center, can be used as augmented data for the training process [35].

4. Conclusion

In conclusion, we proposed a novel scheme exploiting inverse design to manipulate high-dimensional OAM entanglement. The proposed method is implemented using a physic-informed model combined with the overlap integral, allowing us to effectively find optimal solutions for generating target entangled states. Although we have considered the special case of MESs, the inverse design approach is a universal tool to control quantitatively and arbitrarily the distributions of coincidence probability. While there are still challenges in improving experimental

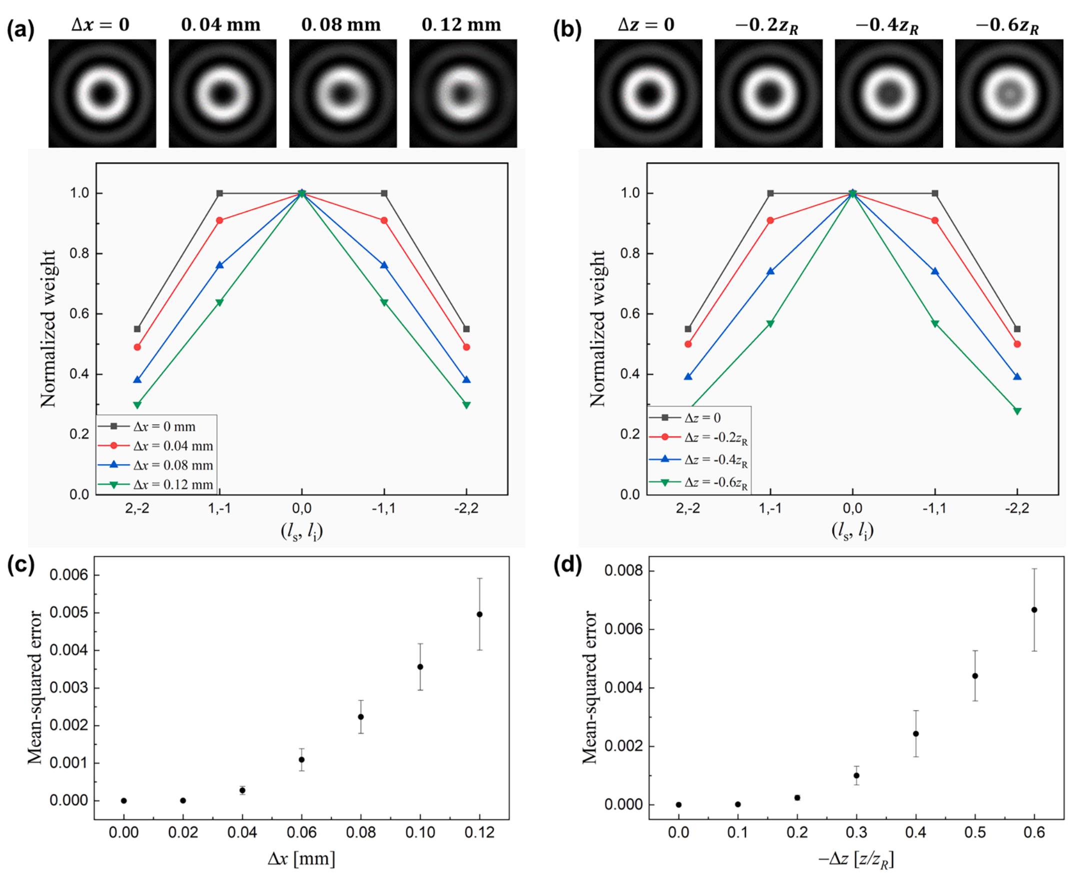

Fig. 6. Performance degradation by optical misalignment. Influence of (a) lateral displacement of the beam center from the diffractive mask and (b) axial displacement of the nonlinear crystal from the lens focal plane. Each inset displays pump intensity profiles being formed at the crystal plane. (c), (d) Changes in MSE values of output according to each offset. Here, normalization was performed by $|c_{l_s,l_i}|^2/|c_{0,0}|^2$.

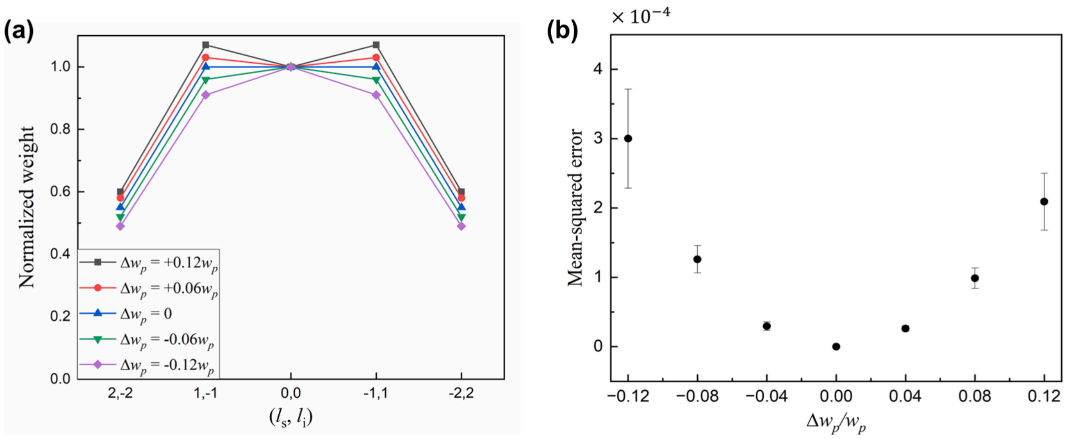

Fig. 7. Performance degradation by different beam sizes. (a) OAM spectrum and (b) calculated MSE values. Here, normalization was performed by $|c_{l_s,l_i}|^2/|c_{0,0}|^2$.

performance, our approach has key advantages. Since the underlying physical principles remain consistent, it is easily extended to higher-dimensional qudit states, and one can handle two independent spatial degrees of freedom, e.g., radial and azimuthal modes, simultaneously. Furthermore, the current single-layer architecture can be extended to a diffractive deep neural network (DDNN) with multiple layers to solve complex problems. Once the DDNN system is completely developed, it is integrated with other optical units, establishing a unified device for advanced tasks. Indeed, a recent study has reported high-dimensional quantum gates implemented by DDNNs [36]. Integrating such gate operations with our DDNN-based quantum state generation scheme presents a promising path toward fully optical quantum circuits. This unified architecture can reduce system errors, enhance stability, and support dynamic reconfiguration for diverse quantum algorithms. The proposed inverse design technique, with its high customizability for spatial degrees of freedom, thus offers a versatile and programmable photonic platform for high-dimensional quantum information processing.

CREediT author contribution statement

Youngbin Na: Conceptualization, Methodology, Software, Investigation, Formal analysis, Data curation, Visualization, Writing – Original Draft. **Do-Kyeong Ko:** Supervision, Funding acquisition, Conceptualization, Methodology, Formal analysis, Writing-Review and Editing.

Declaration of competing interest

The authors declare that they have no known competing financial interests or personal relationships that could have appeared to influence the work reported in this paper.

Acknowledgments

This research was supported by the National Research Foundation of Korea (NRF) grant funded by the Korea government (MSIT) (No. NRF-2021R1A2C2093138); and the AI-based GIST Research Scientist Project grant and Future-leading Specialized Research Project funded by the GIST in 2024 and 2025, respectively.

Data availability

Data will be made available on request.

References

[1] T. Durt, D. Kaszlikowski, J.-L. Chen, L.C. Kwek, Security of quantum key distributions with entangled qudits, Phys. Rev. A 69 (2004) 032313, https://doi.org/10.1103/PhysRevA.69.032313.
[2] S. P. Walborn, D. S. Lemelle, M. P. Almeida, and P. H. Souto Ribeiro, Quantum key distribution with higher-order alphabets using spatially encoded qudits, Phys. Rev. Lett. 96 (2006) 090501, Doi: 10.1103/PhysRevLett.96.090501.
[3] A.C. Dada, J. Leach, G.S. Buller, M.J. Padgett, E. Andersson, Experimental high-dimensional two-photon entanglement and violations of generalized bell inequalities, Nat. Phys. 7 (2011) 677–680, https://doi.org/10.1038/nphys1996.
[4] M. Erhard, M. Krenn, A. Zeilinger, Advances in high-dimensional quantum entanglement, Nat. Rev. Phys. 2 (2020) 365–381, https://doi.org/10.1038/s42254-020-0193-5.
[5] A. Vaziri, G. Weihs, A. Zeilinger, Experimental two-photon, three-dimensional entanglement for quantum communication, Phys. Rev. Lett. 89 (2002) 240401, https://doi.org/10.1103/PhysRevLett.89.240401.
[6] M. Krenn, J. Handsteiner, M. Fink, A. Zeilinger, Twisted photon entanglement through turbulent air across Vienna, Proc. Natl. Acad. Sci. u.s.a. 112 (2015) 14197–14201, https://doi.org/10.1073/pnas.1517574112.
[7] M. Mirhosseini, O.S. Magana-Loaiza, M.N. O'Sullivan, B. Rodenburg, M. Malik, M. P.J. Lavery, M.J. Padgett, D.J. Gauthier, R.W. Boyd, High-dimensional quantum cryptography with twisted light, New J. Phys. 17 (2015) 033033, https://doi.org/10.1088/1367-2630/17/3/033033.
[8] M. Krenn, M. Hunber, R. Fickler, R. Lapkiewicz, S. Ramelow, A. Zeilinger, Generation and confirmation of a (100 × 100)-dimensional entangled quantum system, Proc. Natl. Acad. Sci. u.s.a. 111 (2014) 6243–6247, https://doi.org/10.1073/pnas.1402365111.
[9] L. Allen, M.W. Beijersbergen, R. Spreeuw, J. Woerdman, Orbital angular momentum of light and the transformation of laguerre-Gaussian laser modes, Phys. Rev. A 45 (1992) 8185–8189, https://doi.org/10.1103/PhysRevA.45.8185.
[10] A. Mair, A. Vaziri, G. Weihs, A. Zeilinger, Entanglement of the orbital angular momentum states of photons, Nature 412 (2001) 313–316, https://doi.org/10.1038/35085529.
[11] S. Franke-Arnold, S.M. Barnett, M.J. Padgett, L. Allen, Two-photon entanglement of orbital angular momentum states, Phys. Rev. A 65 (2002) 033823, https://doi.org/10.1103/PhysRevA.65.033823.
[12] F.S. Roux, Y. Zhang, Projective measurements in quantum and classical optical systems, Phys. Rev. A 90 (2014) 033835, https://doi.org/10.1103/PhysRevA.90.033835.
[13] J. Pinnell, I. Nape, B. Sephton, M.A. Cox, V. Rodriguez-Fajardo, A. Forbes, Modal analysis of structured light with spatial light modulators: a practical tutorial, J. Opt. Soc. Am. A 37 (2020) C146–C160, https://doi.org/10.1364/JOSAA.398712.
[14] J. P. Torres, A. Alexandrescu, and L. Torner, Quantum spiral bandwidth of entangled two-photon states, Phys. Rev. A 68 (2003) 050301(R), Doi: 10.1103/Phys. Rev. A.68.050301.
[15] C.H. Bennett, H.J. Bernstein, S. Popescu, B. Schumacher, Concentrating partial entanglement by local operations, Phys. Rev. A 53 (1996) 2046–2052, https://doi.org/10.1103/PhysRevA.53.2046.
[16] A. Vaziri, J.-W. Pan, T. Jennewein, G. Weihs, A. Zeilinger, Concentration of higher dimensional entanglement: qutrits of photon orbital angular momentum, Phys. Rev. Lett. 91 (2003) 227902, https://doi.org/10.1103/PhysRevLett.91.227902.
[17] M. Krenn, A. Hochrainer, M. Lahiri, A. Zeilinger, Entanglement by path identity, Phys. Rev. Lett. 118 (2017) 080401, https://doi.org/10.1103/PhysRevLett.118.080401.
[18] J. Kysela, M. Erhard, A. Hochrainer, M. Krenn, A. Zeilinger, Path identity as a source of high-dimensional entanglement, Proc. Natl. Acad. Sci. u.s.a. 117 (2020) 26118–26122, https://doi.org/10.1073/pnas.2011405117.

[19] E.V. Kovlakov, I.B. Bobrov, S.S. Straupe, S.P. Kulik, Spatial bell-state generation without transverse mode sub subspace postselection, Phys. Rev. Lett. 118 (2017) 030503, https://doi.org/10.1103/PhysRevLett.118.030503.
[20] E.V. Kovlakov, S.S. Straupe, S.P. Kulik, Quantum state engineering with twisted photons via adaptive shaping of the pump beam, Phys. Rev. A 98 (2018), https://doi.org/10.1103/PhysRevA.98.060301.
[21] S. Liu, Z. Zhou, S. Liu, Y. Li, Y. Li, C. Yang, Z. Xu, Z. Liu, G. Guo, B. Shi, Coherent manipulation of a three-dimensional maximally entangled state, Phys. Rev. A 98 (2018) 062316, https://doi.org/10.1103/PhysRevA.98.062316.
[22] S. Liu, Y. Zhang, C. Yang, S. Liu, Z. Ge, Y. Li, Y. Li, Z. Zhou, G. Guo, B. Shi, Increasing two-photon entangled dimensions by shaping input-beam profiles, Phys. Rev. A 101 (2020) 052324, https://doi.org/10.1103/PhysRevA.101.052324.
[23] X. Lin, Y. Rivenson, N.T. Yardimci, M. Veli, Y. Luo, M. Jarrahi, A. Ozcan, All-optical machine learning using diffractive deep neural networks, Science 361 (2018) 1004–1008, https://doi.org/10.1126/science.aat8084.
[24] H. Chen, J. Feng, M. Jiang, Y. Wang, J. Lin, J. Tan, P. Jin, Diffractive deep neural networks at visible wavelengths, Engineering 7 (2021) 1483–1491, https://doi.org/10.1016/j.eng.2020.07.032.
[25] Y. LeCun, Y. Bengio, G. Hinton, Deep learning, Nature 521 (2015) 436–444, https://doi.org/10.1038/nature14539.
[26] Y. Na, D.-K. Ko, Adaptive demodulation by deep-learning-based identification of fractional orbital angular momentum modes with structural distortion due to atmospheric turbulence, Sci. Rep. 11 (2021) 23505, https://doi.org/10.1038/s41598-021-03026-z.
[27] Y. Na, D.-K. Ko, Comparison of Gaussian and vortex probe beams for deep-learning-based turbulence correction, Optik 308 (2024) 171839, https://doi.org/10.1016/j.ijleo.2024.171839.
[28] A. Graves, Generating sequences with recurrent neural networks, Preprint at (2013), https://doi.org/10.48550/arXiv.1308.0850.
[29] T.W. Clark, R.F. Offer, S. Franke-Arnold, A.S. Arnold, N. Radwell, Comparison of beam generation techniques using a phase only spatial light modulator, Opt. Express 24 (2016) 6249–6264, https://doi.org/10.1364/OE.24.006249.
[30] D.F.V. James, P.G. Kwiat, W.J. Munro, A.G. White, Measurement of qubits, Phys. Rev. A 64 (2001) 052312, https://doi.org/10.1103/PhysRevA.64.052312.
[31] E. Toninelli, B. Ndagano, A. Vallés, B. Sephton, I. Nape, A. Ambrosio, F. Capasso, M.J. Padgett, A. Forbes, Concepts in quantum state tomography and classical implementation with intense light: a tutorial, Adv. Opt. Photon. 11 (2019) 67–134, https://doi.org/10.1364/AOP.11.000067.
[32] J.P. Torres, Y. Deyanova, L. Torner, G. Molina-Terriza, Preparation of engineered two-photon entangled states for multidimensional quantum information, Phys. Rev. A 67 (2003) 052313, https://doi.org/10.1103/PhysRevA.67.052313.
[33] E. Cubuk, B. Zoph, D. Mane, V. Vasudevan, Q. Le, AutoAugment: Learning augmentation strategies from data, proc. IEEE conf. comput. Vis, Pattern Recognit (2019) 113–123, https://doi.org/10.1109/CVPR.2019.00020.
[34] Z. Mao, H. Yu, M. Xia, S. Pan, D. Wu, Y. Yin, Y. Xia, J. Yin, Broad bandwidth and highly efficient recognition of optical vortex modes achieved by the neural-network approach, Phys. Rev. Appl. 13 (2020) 034063, https://doi.org/10.1103/PhysRevApplied.13.034063.
[35] P. Wang, W. Xiong, Z. Huang, Y. He, Z. Xie, J. Liu, H. Ye, Y. Li, D. Fan, S. Chen, Orbital angular momentum mode logical operation using optical diffractive neural network, Photon. Res. 9 (2021) 2116–2124, https://doi.org/10.1364/PRJ.432919.
[36] Q. Wang, J. Liu, D. Lyu, J. Wang, Ultrahigh-fidelity spatial mode quantum gates in high-dimensional space by diffractive deep neural networks, Light Sci. Appl. 13 (2024) 10, https://doi.org/10.1038/s41377-023-01336-7.